Indian Journal of Chemical Technology
Vol. 29, November 2022 pp. 658-667
DOI: 10.56042/ijct.v29i6.67390

Solvothermal synthesis and characterization studies of selenium decorated reduced graphene oxide supported $CuSe_2$ nanoparticles as efficient electrochemical catalyst for oxygen reduction reaction

P Ajith, J Agnes, M Sappani Muthu & D Prem Anand*

Department of Physics, St. Xavier's College (Autonomous), Palayamkottai 627 002, Tamil Nadu, India
Affiliated to Manonmaniam Sundaranar University, Abishekapatti 627 012, India

E-mail: mosesajith96@gmail.com

Received 19 August 2022; accepted 21 October 2022

In the energy conversion system, oxygen reduction reaction (ORR) is one of the most significant reactions. Pt-based catalysts are commonly used in fuel cells; the replacement with low-cost materials like transition metal oxides is much needed for the wide application of fuel cells. In this paper, the effective synthesis of copper selenide nanoparticles with selenium-reduced graphene oxide has been described. To establish the existence of selenium, graphene, and copper in manufactured samples, X-Ray diffraction analysis (XRD) has been used. Additionally, fourier transform infrared analysis (FTIR) has been used to examine the functional groups. The structure and morphology have been studied under the scanning electron microscope. UV has been used to assess the synthetic nanoparticles' optical performance. The Brunauer-Emmett-Teller (BET) and Barrett-Joyner-Halenda (BJH) methods have been used to analyze their specific surface area and pore size. Cyclic voltammetry has been used to evaluate the produced nanoparticles' electrochemical performance (CV, LSV).

Keywords: BET, Catalysts, Copper, CV, Oxygen reduction reaction

Researchers have been driven to explore environmentally friendly sustainable energy as a result of the problems caused by the depletion of conventional fossil fuels and changes in the global climate[1]. Due to its great efficiency, easy operation, low emissions, and most importantly unlimited access to renewable reactants, fuel cells are regarded as a sustainable source of energy[2]. The main area of fuel cell technology includes transportation and stationary and portable power[3]. Similar to how batteries do it, the chemical energy of fuels is converted into electrical energy by fuel cells. The most potential alternative to fossil fuels is hydrogen, which is a clean, renewable energy carrier. In this perspective, fuel cells stand out as the most promising energy storage and conversion technologies because they produce electricity directly from the chemical energy of hydrogen[4,5]. Among all types of fuel cells, proton exchange membrane fuel cell (PEMFC) has been investigated for several decades. PEMFCs have drawn interest from all over the world because of their advantages of having a minimal environmental effect, a low operating temperature, and a high energy density. PEMFCs' primary technological component is the oxygen reduction process[6]. The nature of the electrode surface has a significant impact on the reaction. The process involves the generation of oxygen-containing intermediates such as OH, O_2, O, H_2O_2-, and HO_2- in both acidic and alkaline media[7]. The reaction in an aqueous medium is quite reversible. Due to its slow kinetics, ORR is seen from the aspect of electrochemistry as the kinetically limiting component of electrochemical devices[8]. This inspired the development of desired electrocatalysts that could offset the reduction in cell efficiency by getting around the slow kinetics of ORR[9]. The most advanced catalysts for ORR nowadays are still platinum-based (Pt-based) catalysts. Due to their high electrocatalytic activity and stability, superior work function, and high exchange current density, Pt and Pt-based materials have been employed as ORR electrocatalysts[10,11], which, on the other hand, accounts for about 20% of a PEMFC's overall cost and prevents commercialization. Therefore, creating inexpensive catalysts to replace Pt-based catalysts is widely desired[12]. Recently, there are many different non-precious-metal catalysts (NPMCs), but transition metal compound catalysts are particularly challenging

to use in the PEMFC's harsh acid environment. As a result, the PEMFC continues to rely extensively on pt catalysts[13]. Designing the catalyst from the most readily available and affordable materials on Earth is one of the simplest methods to control costs. The earth's crust is abundant in copper, which is also less expensive than most other metals like Ir, Ni, and Co. One of the most significant metals and a component of the coinage is copper. Copper chalcogenides have recently attracted a lot of investigation due to their unique physical, chemical, and semiconducting properties, which are regulated by their chemical composition and crystalline structure and are adaptable by close control of synthesis circumstances[14]. In contrast to iron, cobalt, and nickel, it cannot alloy with lithium like zinc and is monovalent in many combinations. Electrodeposition and hydrothermal processes make it simple to synthesize copper and its selenide[15]. Despite its cheaper cost, earth's abundance, and semiconducting properties, it has a variety of uses in photodetectors, superionic conductors, and solar cells. Excess oxygen-containing functional groups can reduce these systems' electrochemical performance and electrochemical stability of these systems, making them sensitive to chemical oxidation and lowering the long-term durability of all carbon materials[16]. Reduced GO (rGO) is the most widely used and accessible. Reduced graphene oxide has a high specific surface area and functions as a two-dimensional platform for metallic nanoparticles, both of which are essential for catalysis[17-19]. Combining a catalyst's greater surface area with the mass transfer of reactants on its surface, which is controlled by the catalyst's shape[20], can increase ORR Catalytic activities and stability. As a result, the catalyst's shape is the primary factor that can have a substantial impact on catalytic activity, including selectivity and stability[21]. However, there is no report on the electrochemical properties of copper selenide by the solvothermal method. Hence this article depicts the successfully synthesized Se-rGO assisted $CuSe_2$ via the solvothermal method and also characterized the structural, functional, morphological, optical, and electrochemical properties.

Experimental Section

The materials used to synthesize the nanoparticles were purchased from various chemical agencies and laboratories, Selenium oxide ($SeO_{2)}$, and Graphite oxide powder was collected from Ponmani Chemicals Industries, and the reducing agent hydrazine hydrate was obtained from United Scientific Supplies. The Sodium Selenite (Na_2SeO_3), Diethylene Triamine (DETA), and $(CH_3COO)_2$ Cu. H_2O was purchased from spectrum Chemie Pvt. Ltd, all these chemicals were ranked with analytical reagents grade.

Synthesis of Se-rGO

Graphite oxide (200 mg) was ultrasonically dissolved in 100 mL of deionized water at 45°C, and then 200 mg of selenium oxide was added while the mixture was being stirred. For two hours, the temperature was held at 80°C. After then, hydrazine hydrate, a reducing agent, was added to the concoction. The mixture was then filtered with whatman paper, and the ready sample was thoroughly cleaned with deionized water before being freeze-dried. The sample was labeled as Se-rGO[22] (Fig. 1).

Preparation of $CuSe_2$ supported Se-rGO($CuSe_2$/Se-rGO)

Solution A was prepared by dissolving 0.023g of Na_2SeO_3 in 13 mL of Diethylene Triamine (DETA) solution together with 0.1350 g of Se-rGO and 0.0172 g of $(CH_3COO)_2$ Cu. H_2O and 26 mL of water are used to emulsify H_2O to prepare solution B. The two solutions were transferred into an autoclave and kept there for 15 h at 170°C. The system was then allowed to cool until it reached room temperature. The product was thoroughly cleaned with deionized water before being freeze-dried and filtered using Whatman filter paper. The product was labeled as $CuSe_2$/Se-rGO (Fig. 2).

Results and Discussion

On a PAN analytical Xpert 3, X-Ray Diffraction was used to analyze the samples' crystalline nature, phase analysis, and structure of the samples as

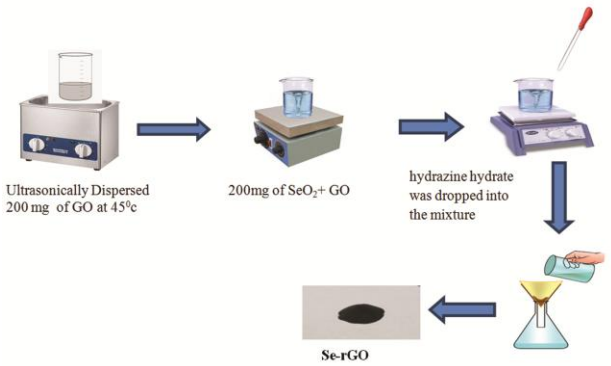

Fig. 1 — Schematic diagram of selenium decorated reduced graphene oxide (Se-rGO).

prepared. An accelerating voltage of 40 kV current of 15 mA with Cu Kα radiation (λ= 1.5406 Å) over the range of 2θ= 20^0 - 90^0. The prominent diffraction peak detected at the diffraction angle and in good agreement with the cubic $CuSe_2$ demonstrates that the diffraction peak is sharp and narrow, indicating that the sample possesses good crystallinity.

No other impurity phases were detected, confirming the very high purity of the obtained $CuSe_2$/Se-rGO sample. Figure 3(a) shows the

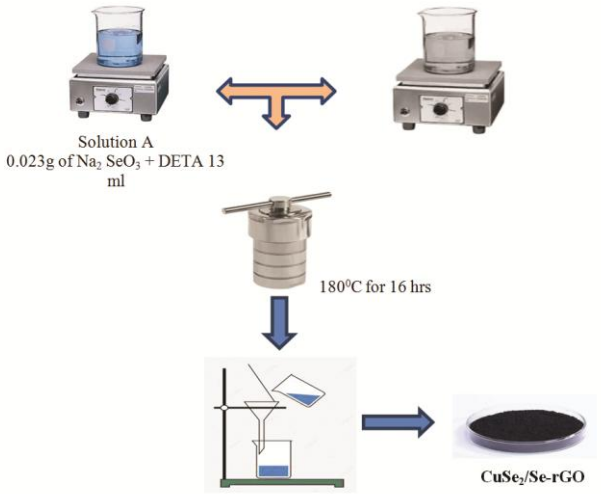

Fig. 2 — Schematic diagram of $CuSe_2$ supported Se-rGO ($CuSe_2$/Se-rGO).

X-Ray Diffraction pattern of prepared CuSe2/Se-rGO nanoparticles. The Diffraction pattern of as-synthesized $CuSe_2$/Se-rGO nanoparticles showing a series of diffraction peaks at 26^0, 29^0, 33^0, 36^0, 50^0,54^0, 57^0 corresponds to 111, 200, 210, 211, 311, 230, 321 planes. The main diffraction peak of the synthesized nanoparticle presents a sharp peak value and the position of diffraction peaks coincide with the standard card of (JCPDS No.26-1115)[23]. The strongest peak of the $CuSe_2$/Se-rGO sample was found at position 26.3614^0, corresponding to the (111) plane. A broad peak appears at 2θ ~29.8005 confirming the reduction of GO in a composite[24]. The peak position at 2θ = 33, 44 confirms the presence of selenium and the peak between 20^0 to 24^0 shows the presence of graphene. Knowing the peak's full width at half maximum (FWHM) (β), wavelength (λ), and diffracting angle (θ), Using Debye Scherrer's formula (Equation1), the crystalline size "D" of the produced nanoparticles was determined.

$$D = k\lambda/\beta\ cos\theta \qquad \ldots(1)$$

where, k is a constant = 0.9, λ is the wavelength =1.5406Å, β = full width at half maxima and θ is Bragg angle[25], the calculated average crystalline size was 18 nm. The dislocation density $\sigma = 1/D^2$, the calculated dislocation density of the prepared $CuSe_2$/Se-rGO nanoparticle is 0.003086.

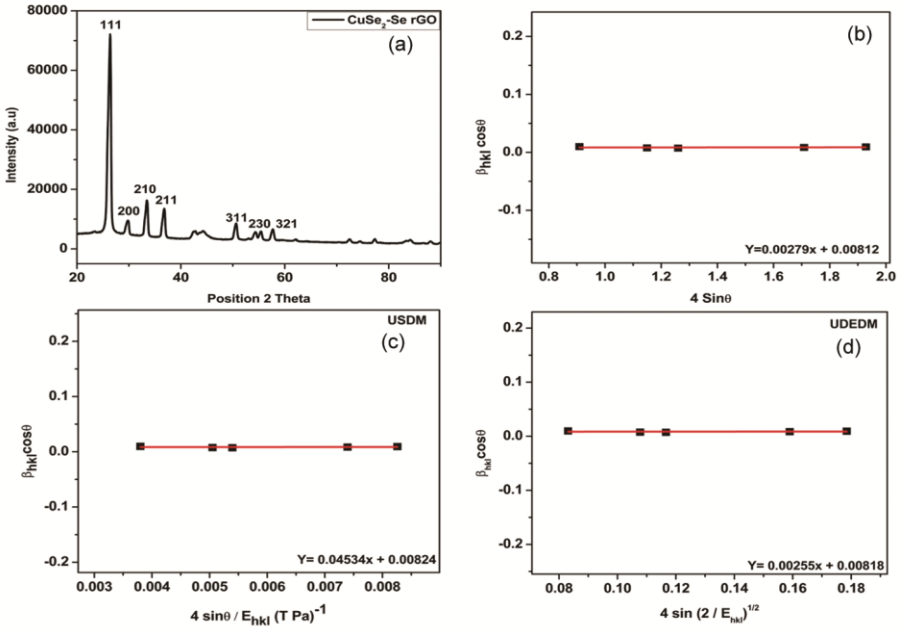

Fig. 3 — (a) XRD pattern; (b) UDM plot; (c) USDM plot and (d) UDEDM plot for $CuSe_2$/Se-rGO.

Williamson-Hall method

The method was used to determine the strain brought on by crystal flaws and distortion in powders.

$$\varepsilon = \beta_s/4\tan\theta \quad \ldots(2)$$

It is established by Equations 1 and 2 that peak width varies with crystallite size as 1⁄cosθ and strain as tanθ. Because of this fundamental distinction, size and strain broadening can be added together to make up the complete integral breadth of a Bragg peak[26].

$$\beta_{hkl} = \beta_S + \beta_D \quad \ldots(3)$$

$$\beta_{hkl} = (4\varepsilon\tan\theta) + (K\lambda/D\cos\theta) \quad \ldots(4)$$

Rearranging Equation. 4 gives

$$\beta_{hkl}\cos\theta = (k\lambda/D) + (4\varepsilon\sin\theta) \quad \ldots(5)$$

Figure 3(b) shows the uniform deformation model (UDM) of the prepared sample. A plot is drawn with $4\sin\theta$ along the x-axis and $\beta_{hkl}\cos\theta$ along the y-axis [Fig. 3(b)]. The crystalline size and strain were estimated from the y-intercept and slope of the linear fit to the data, respectively. The UDM, which considers the crystal's isotropic nature and the fact that material properties are unaffected by the direction in which they are measured, is shown in Equation 5. In all crystallographic directions, it was expected that the strain would be uniform. Straight correspondence between stress and strain is described as a simplified Hooke's law, as given by $\sigma = Y\varepsilon$, where σ is the stress and Y is Young's modulus. Applying the Hooke's law approximation to Equation 5 yield the following Equation 6

$$\beta_{hkl}\cos\theta = (k\lambda/D) + (4\sigma\sin\theta/Y_{hkl}) \quad \ldots(6)$$

As illustrated, Fig. 3(c), it shows the Uniform Stress Deformation Model (USDM) of the prepared sample, the uniform stress can be determined from the intercept and crystallite size from the slope line plotted between $4\sin\theta/Y_{hkl}$ and $\beta_{hkl}\cos\theta$. If Y_{hkl} of cubic, nanoparticles are known, strain can be measured using Equation 6, which represents USDM. Y_{hkl} is associated with the elastic compliances of the samples that have a cubic crystal phase. S_{ij} is given as followed:

$$1/Y_{hkl} = S_{11} - 2[(S_{11} - S_{12}) - 1_2 S_{44}](l^2m^2 + m^2n^2 + n^2l^2) \quad \ldots(7)$$

where l, m, n are the cosines of the angles between Y's direction and the crystal axes[27] and S_{11}, S_{12}, S_{44} are the elastic compliances of $CuSe_2$/Se-rGO nanoparticles. As it relates to their elastic stiffness, S_{11}, S_{12}, S_{44} are as follows:

$$C_{14} = 1/S_{44}, C_{11} - C_{12} = (S_{11} - S_{12})^{-1}, C_{11} - 2C_{12} = (S_{11} - 2S_{12})^{-1} \quad \ldots(8)$$

For spinel ferrite, the elastic stiffness C_{11}, C_{12}, C_{44} values are 275 GPa, 104 GPa, and 95.5 GPa, respectively[28,29]. Both of these samples as well as all spinel ferrites share these values. The homogeneity and isotropy assumptions in Equation 6 are unjustified. Additionally, when the strain energy density u is taken into account, the constants of proportionality related to the stress-strain relation are no longer independent. Hooke's law states that the energy density is determined by strain and is estimated from the following Equation 9.

$$u = (\varepsilon^2 Y_{hkl})/2 \quad \ldots(9)$$

Equation 6 was modified as follows:

$$\beta_{hkl}\cos\theta = (k\lambda/D) + (4\,sin\theta\,(2u/Y_{hkl})^{1/2} \ldots(10)$$

The data were fitted to a plot of $\beta_{hkl}\cos\theta$ versus $4\,sin\theta\,(2u/Y_{hkl})^{1/2}$ and the plot was created. Figure 3(d) shows the Uniform Deformation Energy Density Model (UDEDM) of the prepared sample, using the y -intercept and slope, the crystallinity and directional power density were estimated. Equation (10) is illustrated in Fig. 3(d) and represents UDEDM. The calculated values for crystallite size, stress, power density, and strain were shown in Table 1.

The FTIR spectra for all prepared samples are analyzed using Bruker, Alpha T, and model spectrometer, the sample was vacuum dried and ground with KBr to form a pellet which was then analyzed from the range of 400 to 4000 cm^{-1} [30,31]. The spectra confirms the characteristic vibrations and functional groups present in the samples. Figure 4

Table 1 — Calculated values of crystallite size, power density, and strain from various method.

Scherrer formula	W-H method								
	UDM		USDM			UDEDM			
D (avg) nm	D (nm)	ε × 10^{-3} (no unit)	D (nm)	ε × 10^{-3} (no unit)	σ (MPa)	D (nm)	ε × 10^{-3} (no unit)	σ (MPa)	u KJ/m^3
18	17	2.79	17.5	0.1966	0.212	17.7	0.2375	0.0547	.00065

shows the Fourier Transform Infrared spectra of $CuSe_2$/Se-rGO. The wavelength at 1609 cm^{-1} assigns the presence of CU^{2+} ions[32], and the wavelength at 3471 cm^{-1} corresponds to N-H stretching vibration band (which can be attributed to the interaction of N_2H_4 with copper ions), the wavelength at 3399 cm^{-1} and 1422 cm^{-1} confirm the O-H characteristic vibrations[33]. The wavelength at 2924 cm^{-1} corresponds to N-H stretching vibration band. The wavelengths at 547 and 3747 cm^{-1} confirm the Cu-O stretching and O-H bonds[34].

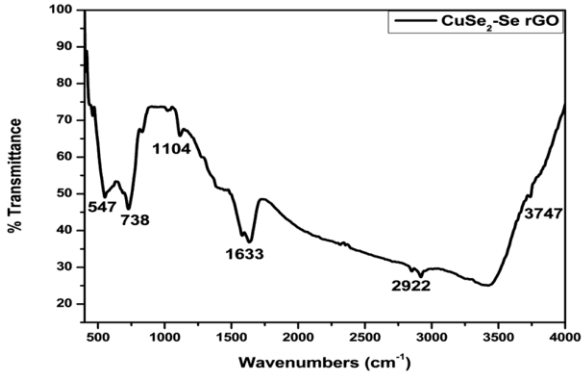

Fig. 4 — FTIR spectra of prepared $CuSe_2$/Se-rGO nanomaterial.

An apparatus is used for scanning electron microscopy to examine topographic specimens with extremely high magnification. Using a Carl Zeiss EVO 18 at a 25 Kx magnification, an SEM examination was performed. The major purpose of SEM is to determine the general morphology of nanocomposites at sizes ranging from several microns to 500 nm. The morphology of the synthesized $CuSe_2$/Se-rGO nano materials examined by the SEM was shown in Fig. 5, the images were taken at various magnification sizes (1µm, 2 µm, and 200 nm) the images show the flake structure at the magnification of 2µm and 200 nm.

The UV-absorption bands and Tauc's plot of the synthesized $CuSe_2$/Se-rGO nanoparticles are shown in Figs 6 (a and b). A solution's absorbance (A) is used to calculate how much light it has absorbed, often referred to as optical density (OD). At 279 nm, the absorption peak has been reached. The transition of an electron from a non-bonding orbital to an antibonding π^* orbital is referred to as the $n \rightarrow \pi^*$ conversion. Components containing hetero atoms in double bonds (C=O, C≡N, and N=O) go through this transition; it requires the least amount of energy and exhibits absorption at a longer wavelength of about 300 nm[35].

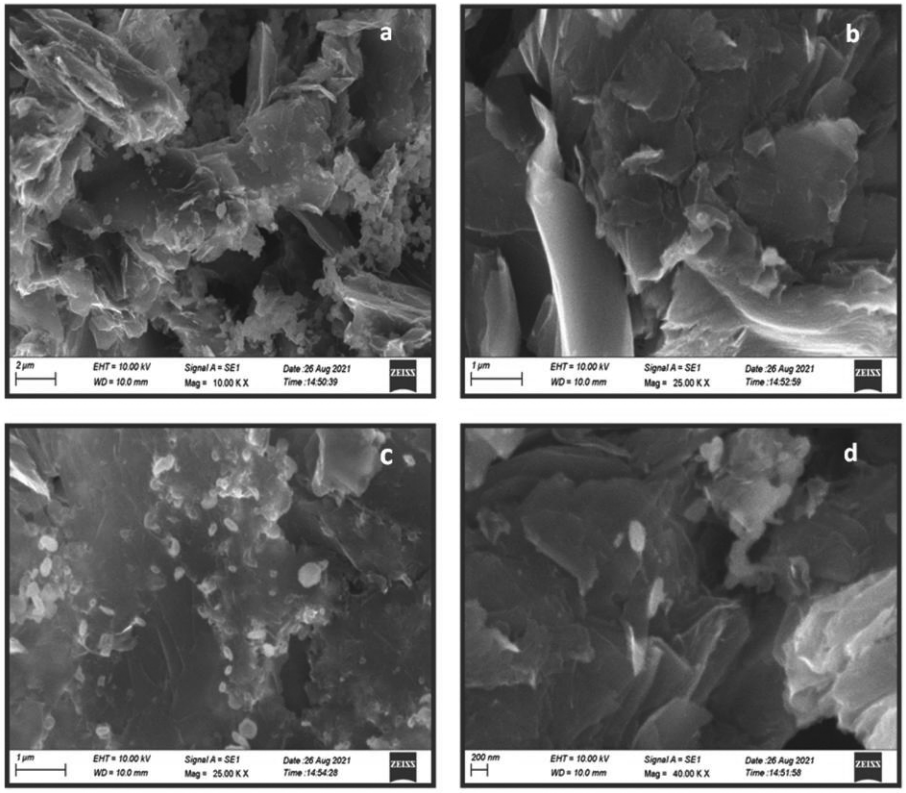

Fig. 5 — SEM images of prepared $CuSe_2$/Se-rGO taken at different magnifications of (a) 2µm; (b) and (c) 1 µm and (d) 200 nm respectively.

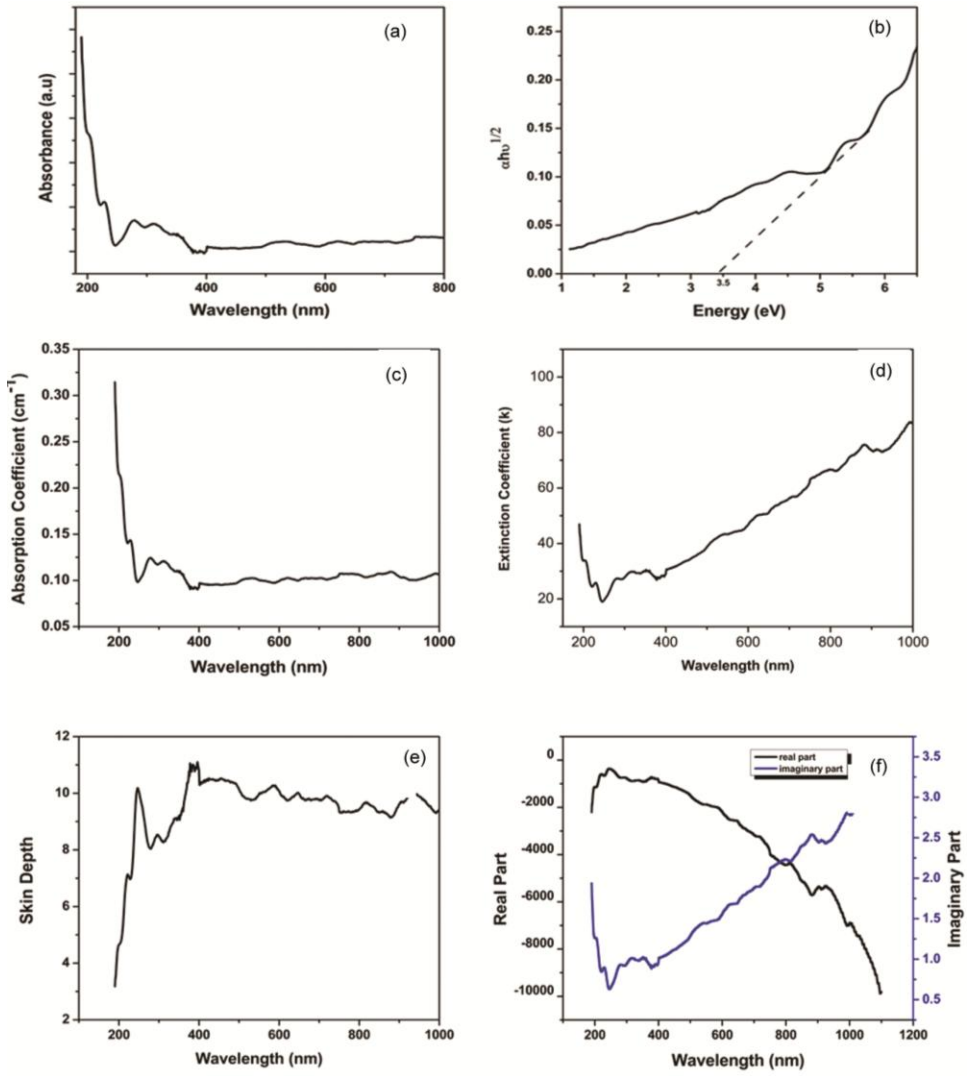

Fig. 6 — (a) Absorbance; (b) Tauc's plot; (c) Absorption coefficient; (d) Extinction coefficient; (e) Skin depth and (f) Dielectric constant of synthesized CuS_{e2}/Se-rGO.

The samples' optical band gap energy (Eg) was estimated using the equation shown below:

$$(\alpha h\nu)^n = A\,(h\nu - Eg) \qquad \ldots(11)$$

where A is constant, ν represents the wavelength of light, Eg denotes the material's energy bandgap, α indicates the absorption coefficient, h denotes the Plank's constant, and the exponent n factor's value depends on the kind of electron transition. For indirect bandgap and allowed transition n=1/2; for direct transition n=2; and directly forbidden transition n=3/2.

The calculated bandgap energy for the prepared $CuSe_2$/Se-rGO nanoparticles is 3.5 eV based on Tauc's plot $[(\alpha h\nu)^{1/2}$ vs hν]. The literature review states that the copper selenide's band gap is about 2.7 eV[36]. Therefore, it was found that copper selenide with rGO enhanced the band gap. Figure 6(c) shows the absorption coefficient of the prepared sample. The absorption coefficient is influenced by both the substance and the wavelength of the light being absorbed, a material's capacity to absorb light at a certain thickness[37]. The prepared reduced graphene oxide nanoparticle's highest absorbance was measured at 189 nm. So that it can more successfully absorb light of a 280 nm wavelength. Additionally, it was noted that the graph has an odd tendency, initially decreasing and then slightly increasing before becoming straight [Fig. 6(c)]. It demonstrates that the material's internal electric field, the absorption coefficient is calculated using the equation given below,

$$\propto = \frac{2.303 * A}{l} \qquad \ldots(12)$$

where A defines the absorbance (280 nm), and cuvette length (1 cm).

The wavelength of light affects how much of it a substance or material can absorb. The produced material's chemical composition and structural makeup determine it. The study of electromagnetic radiation scattering loss and material absorption is known as the extinction coefficient.

Absorption: $K = \frac{\propto\lambda}{4\Pi}$ …(13)

where, the λ is the wavelength, and α is the coefficient in Fig. 6. After 380 nm, the extinction coefficient progressively increases and then briefly declines and increases as the wavelength increases.

The optical penetration depth is the maximum depth to which electromagnetic radiation, including light, can pass through a substance. Figure 6(e) shows the skin depth of the prepared sample. From Fig. 6(e), it can be seen that skin depth initially increases up to 246 nm before decreasing.

Skin depth $\delta = \frac{1}{\alpha}\alpha$ is the absorption coefficient. Skin depth peaked at 386 nm after starting at a minimal value of roughly 311 nm. This demonstrates how the material is being penetrated deeper and deeper by electromagnetic radiation with wavelengths of about 397 nm.

A dielectric constant that is proportional to the density of states in the forbidden energy gap, is used to calculate a substance's permittivity and polarizability. The real part of the dielectric constant determines how rapidly light can be decelerated inside a substance. The energy that an electric field absorbs due to dipole motion is indicated by the imaginary portion.

Dielectric Constant

Real Part $A = \pi r^2 = n^2 - k^2$, …(14)

Imaginary part $\varepsilon_i = 2nk$ …(15)

where n represents the Refractive Index and k denotes the Extinction coefficient, The prepared sample's dielectric constant is shown in Fig. 6(f) , The imaginary part's maximum value is 1100 nm, which was caused by the material's electric field, and the minimum value is 245 nm. The greatest absorption is shown at the real part's peak value of 248 nm, while the real part's lowest is 1102 nm.

The Smart Sorb 93Ins. N_2 adsorption-desorption isotherm was used to assess the volume and pore size of the prepared $CuSe_2$/Se-rGO material [Fig. 7(a)]. The catalyst exhibits a type II N_2 isotherm at 98.138 KPa, which is classified by IUPAC as a macroporous feature of $CuSe_2$-SerGO microspheres[38] and indicates the existence of mesopores with an H4 hysteresis loop. Adsorbent and adsorbate equilibrium relationships are described by isotherms.

Total Surface Area S_t = (WNA)/M, …(16)

where N is known as the Avogadro no, M denotes the molecular weight of an adsorbate, W is defined as

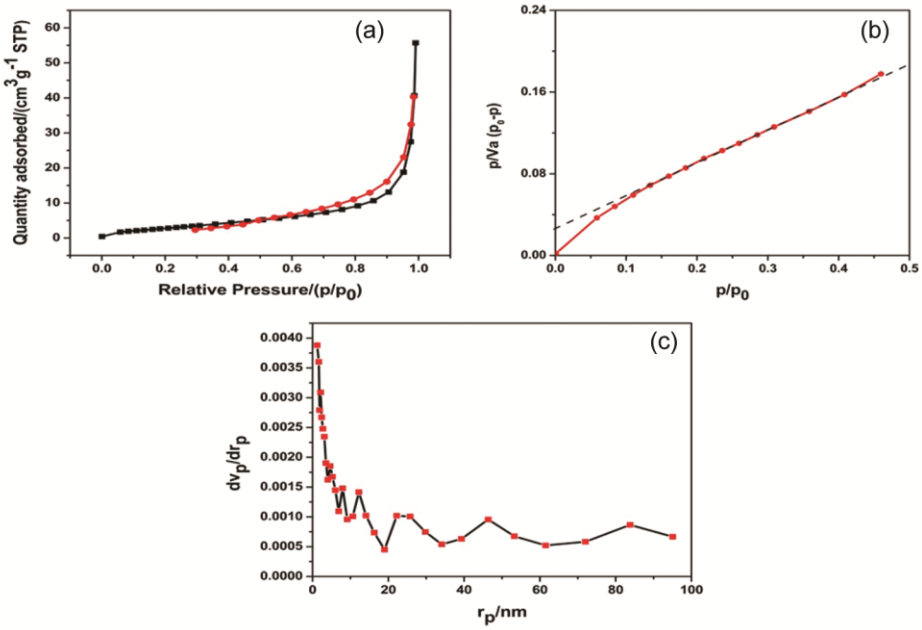

Fig. 7 — Graph of synthesized CuS_{e2}/Se-rGO (a) Abs-Des isotherm; (b) BET and (c) BJH.

the weight of the monolayer, and the A stands for the cross-sectional area of the adsorbate. From the N_2 ads/des isotherm in Fig. 7(b) the surface area of the catalyst is 1.2300E+01 m^2g^{-1}, variables such as how materials decompose, ignite, and react with other substances are influenced by surface area. The overall pore volume (p/po = 0.9990) is 8.1653 $cm^3\ g^{-1}$ and the monolayer absorbed gas volume *Vm* is 2.8261 cm^3 (STP) g^{-1}, The porous composition can offer additional active sites to enhance the electrocatalyst's ORR performance. An electrocatalyst needs to fulfill several criteria, such as having a distinctive form, having a large surface area, and having produced a sample that is porous[39]. One of the finest methods for determining mesopore size is the BJH method (2-50 nm). Utilizing data on nitrogen adsorption-desorption, this method is specially made to create curves showing how pore volume distribution varies with pore diameter (isotherm).

The synthesized material's BJH- Plot is displayed in Fig. 7(c). The sample weight was 1.57 g, and the study was carried out at 77.000K adsorption temperature and 97.185 KPa of saturated vapor pressure. From the BJH Plot, $r_{p,\ peak}$ (area) is 1.22 nm, the area is 15.524 m^2g^{-1}, and the pore volume Vp is 8.3131E-02 cm^3g^{-1}.

One of the most adaptable and dynamic electroanalytical techniques for evaluating electroactive compounds and their redox processes is cyclic voltammetry. With different solvent-supporting electrolyte combinations, this approach can quickly observe redox behaviour over a wide potential range. This approach can be used to investigate the bulk properties of materials in or on electrodes, the redox activity of molecules that diffuse to a surface of the electrode, and interfacial phenomena at an electrode surface. Given this, the commonly used cyclic voltammetry is a part of the dynamic redox technique class that analyzes the potential given to an electrolytic cell[40]. The output of the cell is current versus potential. A typical three-electrode cell for material research consists of a working electrode, a counter-electrode, and a reference electrode whose potential is known in a particular environment. By monitoring the current at the working electrode throughout the potential scan, a cyclic voltammogram is produced. A depiction of the current flowing through the electrochemical cell during the cyclic potential scan is the result of cyclic voltammetry. Through the use of a potentiostat circuit, the voltage-current curves are monitored. The working electrode potential is maintained at a predetermined value in a three-electrode configuration by managing the potential difference between the working electrode (WE) and the reference electrode (RE). By analyzing the Cyclic Voltammetry in an O_2 and also N_2 saturated, 0.1 M KOH solution alkaline medium at room temperature, the ORR catalytic activity of the prepared sample $CuSe_2$-Se-rGO, was investigated. Glassy Carbon is employed as an electrode and the scan rate for CV is 50 mV/s. N_2 saturated solution has one more observable redox peak than O_2 saturated solution. The oxygen reduction reaction mechanism is indicated by the characteristic cathodic peak. Figure 8 displays the CV graph of the synthesized $CuSe_2$–Se-rGO nanoparticles in O_2 and N_2 saturated solution. The peak potential of the generated sample towards the ORR is determined to be 0.8 v.

Using the provided formula, the prepared sample's specific capacitance is determined as

$$Cp = \frac{A}{2mk\ (V2-V1)} \qquad \ldots(17)$$

where A denotes the area inside the CV curve having units AV., k is known as the scan rate of CV

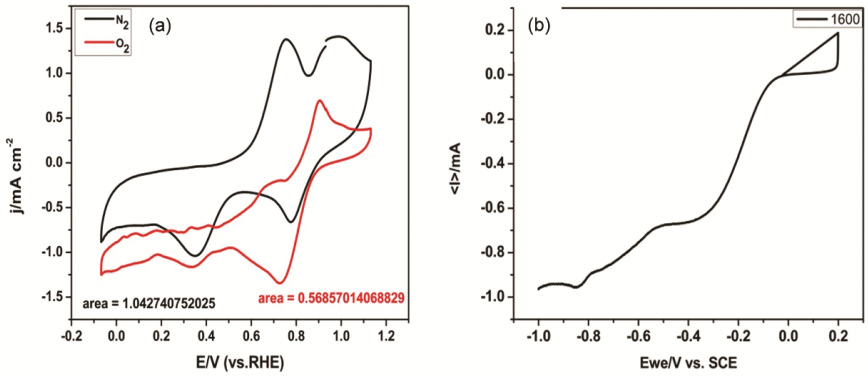

Fig. 8 — (a) Cyclic voltammetry graph and (b) LSV of the $CuSe_2$/Se-rGO.

Table 2 — Computed specific capacitance of the $CuSe_2$/Se-rGO.

Sample	Saturated solution	Area (unit)	Specific capacitance (F/g)
$CuSe_2$/Se-rGO	N_2	1.042740752025	10427.40752025
$CuSe_2$/Se-rGO	O_2	0.185616551	5685.7014068829

(50 mV/s), m denotes the mass of the active material, and (V2 –V1) defines as the potential window. The potential window of CV is 1 (total voltage range). Table 2 lists the computed specific capacitance.

Conclusion

By using the solvothermal approach, copper selenide nanoparticles with selenium-reduced graphene oxide have been successfully produced. The X-ray diffraction analysis has been used to assess the crystal size and phase composition of the nanoparticle. The FTIR analysis has been used to pinpoint the functional groups that were present in the produced sample. The produced samples' morphology and composition have been examined using a scanning electron microscope. UV-Vis spectroscopy has identified the optical absorption and bandgap as being 279nm and 3.5eV. The $CuSe_2$/Se-rGO composite's surface area and pore size are evaluated using the N2 adsorption-desorption isotherm. At 98.138 kPa, the catalyst exhibits a type II N_2 isotherm. By comparing O_2 and N_2 saturated solutions using cyclic voltammetry, it has been discovered that the latter exhibits a more prominent redox peak. It has been established that the $CuSe_2$–Se-rGO is the effective electrochemical catalyst for the ORR, which took place in the N_2 and O_2 - saturated solution.

Acknowledgement

The author acknowledges the support and encouragement of the Principal Rev. Fr. Mariadoss S. J and Secretary Rev. Fr. Pushparaj S. J of St. Xavier's College (Autonomous), Palayamkottai. The author thankful Dr. M. Augustine, Assistant Professor, St. Joseph's College, Trichy, to help with the interpretation of WH data and finally, for the organizing committee of the 2nd ICACSEM-2022, Department of Physical Chemistry, University of Madras, Guindy.

References

1 Yang D, Zhu Q, Chen C, Liu H, Liu Z, Zhao Z & Han B, *Nat Commun*, 10 (2019) 1.
2 Bhuse V M, Hankare P P, Garadkar K M & Khomane A S, *Mate Chem Phys*, 80 (2003) 82.
3 Ellis M W, Von Spakovsky M R & Nelson D J, *Proceedings IEEE*, 89 (2001) 1808.
4 Felseghi R A, Carcadea E, Raboaca M S, Trufin C N & Filote C, *Energies*, 12 (2019) 4593.
5 Singla M K, Nijhawan P & Oberoi A S, *Environ Sci Pollut Res*, 28 (2021) 15607.
6 Lee J M, Han H, Jin S, Choi S M, Kim H J, Seo M H & Kim W B, *Energy Technol*, 7 (2019) 1900312.
7 Zagal J H & Koper M T, *Angewandte Chemie International Edition*, 55 (2016) 14510.
8 Goswami C, Hazarika K K & Bharali P, *Mater Sci Energy Technol*, 1 (2018) 117.
9 Qian Y, Khan I A & Zhao D, *Small*, 13 (2017) 1701143.
10 Brouzgou A, Song S Q & Tsiakaras P, *Appl Catal B: Environ*, 127 (2012) 371.
11 Chen Z, Higgins D, Yu A, Zhang L & Zhang J, *Energy Environ Sci*, *4* (2011) 3167.
12 Long N V, Yang Y, Thi C M, Van Minh N, Cao Y & Nogami M, *Nano Energy*, 2 (2013) 636.
13 Bak S J, Kim S I, Lim S Y, Kim T, Kwon S H & Lee D H, *Int J Mol Sci*, 22 (2021) 12300.
14 Wang J J & Ryan K M, *Cryst Eng Comm*, 18 (2016) 3161.
15 do Nascimento J R, D'Oliveira M R, Veiga A G, Chagas C A & Schmal M, *ACS Omega*, 5 (2020) 25568.
16 Navalon S, Dhakshinamoorthy A, Alvaro M & Garcia H, *Coord Chem Rev*, 312 (2016) 99.
17 Ratnayake S P, Mantilaka M MM G P G, Sandaruwan C, Dahanayake D, Murugan E, Santhosh SKumar S, Amaratunga G A J & Nalin de Silva K M, *Appl Catal A: Gen*, 570 (2019) 23.
18 Santhoshkumar S & Murugan E, *Appl Surf Sci*, 553 (2021) 149544.
19 Murugan E, Govindaraju S & Santhoshkumar S, *Electrochimica Acta*, 392 (2021) 138973.
20 Ratnayake S P, Sandaruwan C, Mantilaka M MM G P G, De Silva N, Dahanayake D, Wanninayake U K, Bandara W R L N, Santhoshkumar S, Murugan E, Amaratunga G A J & Nalin de Silva K M, *J Ind Eng Chem*, 95 (2021) 203.
21 Zhou K & Li Y, *Angew Chem Int Ed*, 51 (2012) 602.
22 Ajith P, Rajkumar A, Muthu M S, Agnes J & Anand P, *Nanjing Youdian Daxue Xuebao (Ziran Kexue Ban)/J Nanjing Univ Posts Telecommun (Nat Sci)* (2021).
23 Yang C T, Hsiang H I & Tu J H, *Adv Powder Technol*, 27 (2016) 959.
24 Kim N H, Kuila T & Lee J H, *J Mater Chem A*, 1 (2013) 1349.
25 Augustin M & Balu T, *Int J Nanosci*, 16 (2017) 1650035.
26 Agnes J, Selvakumar M S & Anand D P, *Mater Today Proc*, 5 (2022) 256.
27 Date E H F & Andrews K W, *J Phys D: Appl Phys*, 2 (1969) 1373.
28 Suriakarthick R, Pandian M S, Ramasamy P, Raji R K, Muralidharan M, Amaljith C K & Sagadevan S, *Inorg Chem Commun*, 140 (2022) 109491.
29 Dimiduk D M, Uchic M D & Parthasarathy T A, *Acta Mater*, 53 (2005) 4065.
30 Murugan E, Santhoshkumar S, Govindaraju S & Palanichamy M, *Spectrochim Acta Part A: Mol Biomol Spectrosc*, 246 (2020) 119036.

31 Murugan E, Santhoshkumar S, Reshna K M & Govindaraju S, *J Mater Sci*, 54 (2019) 5294.
32 Kumar P & Singh K, *Struct Chem*, 22 (2011) 103.
33 Dong Y, Peng Q & Li Y, *Inorg Chem Commun*, 7 (2004) 370.
34 Sangamesha M A, Pushpalatha K & Shekar G L, *Indian J Adv Chem Sci*, 2 (2014) 223.
35 Muthu M S, Xavier S S J, Ajith P & Anand D P, *Mater Today: Proc*, 6 (2022) 367.
36 Ajith P, Agnes J, Muthu M S & Selvakumar M S, *Mater Today: Proc*, 5 (2022) 287.
37 Santhoshkumar S & Murugan E, *Dalton Trans*, 50 (2021) 17988.
38 Tashiro Y, Taniguchi K & Miyasaka H, *Electrochim Acta*, 210 (2016) 655.
39 Xu C, Wei X, Ren Z, Wang Y, Xu G, Shen G & Han G, *Mater Lett*, 63 (2009) 2194.
40 Murugan E, Rubavathy Jaya Priya A, Janaki Raman K, Kalpana K, Akshata C R, Santhosh Kumar S & Govindaraju S, *J Nanosci Nanotechnol*, 19 (2019) 7596.